Modeling of Induction in Integrated Power-Gas Systems Due to Geomagnetic Disturbances

Modeling of Induction in Integrated Power-Gas Systems Due to Geomagnetic Disturbances

Min-zhou Liu, *Graduate Student Member, IEEE,* Yan-zhao Xie, *Senior Member, IEEE,* Yu-hao Chen, Riccardo Trinchero, *Member, IEEE,* and Igor S. Stievano, *Senior Member, IEEE*

***Abstract*—Rigorous evaluation of geomagnetic induction in the integrated power-gas systems (IPGS) is critical for the risk assessment of geomagnetic disturbances (GMD). Existing geomagnetic induction models are developed individually for the power grids or pipeline networks. This paper proposes a nodal voltage analysis method for the geomagnetic induction modeling in the IPGS considering the interaction between the power grids and pipelines. The conductive coupling of grounded nodes in the IPGS, including substation grounding grids and buried pipelines, is modeled with the ground transfer resistance. Several IPGS test cases are used to illustrate the impacts of the interaction on the induced voltages and currents. The influences of spatial patterns and resistance parameters of IPGS as well as earth resistivity structures on the interaction are discussed.**

***Index Terms*—Geomagnetic disturbances, geomagnetically induced currents, ground transfer resistance, integrated power-gas systems, pipe-to-soil potentials.**

I. Introduction

GEOMAGNETIC disturbance (GMD) hazards initiated by space weathers can induce low-frequency (0.1 mHz–0.1 Hz) geoelectric fields on the earth surface, which may pose a threat to the reliability of the ground-based technological systems, including power grids and pipeline networks [1]–[3]. Geomagnetically induced currents (GIC) in power grids could give rise to half-cycle saturation of the transformers, causing hot-spot heating, reactive power loss and harmonic distortion, etc [4]–[12]. The pipe-to-soil potentials (PSP) may accelerate the corrosion of the pipes and interfere with the cathodic protection system [13]–[17].

Nowadays, the integrated power-gas systems (IPGS) are promising for improving the flexibility of energy supply. The power systems and natural gas pipeline networks are increasingly coupled both spatially and functionally, which has not been taken into full account in geomagnetic induction modeling and its effect assessment. On the one hand, common corridors of power lines and buried pipelines have been built to save the land. Thus, the earthing GIC from the power grid and buried pipes may interact with each other, thereby redistributing the induced voltages and currents in the IPGS. On the other hand, natural gas-fired power generation and power-to-gas technology raise the functional dependencies [18]. For instance, the potential transformer outage during a GMD event may lead to cascading failures in the IPGS. Hence, as a first step, rigorous and efficient modeling of geomagnetic induction in the IPGS is of great importance for the GMD risk assessment and mitigation.

In the general context, electromagnetic interference between AC power grids and pipeline networks has attracted much attention, e.g. fault currents [19], harmonic interference [20], [21], lightning strikes [22], and HVDC ground return currents [23]. However, the existing geomagnetic induction models are developed separately for power grids and pipeline networks according to their grounding nature without adequately considering their conductive coupling.

The power grid is *discretely grounded* through the substation grounding grids in the GIC model. For a general power grid with multiple voltage levels, the full-node models, including the Lehtinen-Pirjola method [4], [5] and the nodal admittance matrix method [6], are proposed to calculate the GIC. Furthermore, the bus admittance matrix method [7] and the reduced nodal admittance matrix method [8] are proposed to speed up the GIC computation through model order reduction. In most GIC calculations, the coupling between the substation grounding grids through the earth is usually considered negligible. Some literature analyzed the influence of mutual resistances between substations on GIC in the cases of the uniform earth [9] and horizontally layered earth [10].

On the contrary, the pipelines are *continuously grounded* through the insulation coating in the geomagnetic induction model. Boteler and Cookson [13] first proposed the distributed source transmission line model to calculate the PSP and GIC along the pipeline. For the analysis of large-scale pipeline networks, some efficient equivalent methods have been proposed for pipes, including the Thevenin equivalent circuit [14], the equivalent-pi circuit with uniform geoelectric field [15], and the equivalent-pi circuit with nonuniform geoelectric field [16].

There are two main types of coupling between power grids and pipeline networks during GMD. The first category is *conductive coupling*. The quasi-DC earthing currents from substation grounding grids and pipelines, driven by the geoelectric field, can produce additional electric fields in the soil.

This work was supported by the National Key R&D Program of China under Grant 2016YFC0800100, in part by the China Scholarship Council Foundation under Grant 202006280077, and in part by the Outstanding Chinese and Foreign Youth Exchange Program of China Association for Science and Technology (CAST). *(Corresponding author: Yan-zhao Xie.)*

Min-zhou Liu is with the State Key Laboratory of Electrical Insulation and Power Equipment, School of Electrical Engineering, Xi'an Jiaotong University, Xi'an 710049, China, and also with the Department of Electronics and Telecommunications, Politecnico di Torino, 10129 Turin, Italy (e-mail: liuminzhou@outlook.com).

Yan-zhao Xie and Yu-hao Chen are with the State Key Laboratory of Electrical Insulation and Power Equipment, School of Electrical Engineering, Xi'an Jiaotong University, Xi'an 710049, China (e-mail: yzxie@mail.xjtu.edu.cn; yuhao.chen@mail.xjtu.edu.cn).

Riccardo Trinchero and Igor S. Stievano are with the Department of Electronics and Telecommunications, Politecnico di Torino, 10129 Turin, Italy (e-mail: riccardo.trinchero@polito.it; igor.stievano@polito.it).

Thus, they can generate a potential difference between other grounding bodies. The second type is *inductive coupling* [17]. GIC in the power grid could lead to half-cycle saturation of the transformer, and the resulting harmonics flowing through the overhead power transmission lines can be inductively coupled to adjacent pipelines, which can be evaluated using well-established methods [20], [21]. Hence, this paper focuses on the modeling of conductive coupling in the IPGS.

In summary, the interaction between the earthing currents from substation grounding grids and pipelines is not considered in the classical geomagnetic induction models developed for power grids or pipelines separately. Hence, the classical models are not suitable for the geomagnetic induction analysis of the IPGS, where the AC substation may be very close to the pipeline, e.g. only several hundred meters to several kilometers away. Their conductive coupling is relatively strong in this case, thus the classical models may yield biased estimates of the level of the induced voltages and currents in integrated systems and their effects. It may further lead to the result that the mitigation and protection measures developed on this basis do not match the actual magnitude and spatial distribution of the induction results.

In this respect, we propose a novel geomagnetic induction model for the IPGS. To the best of our knowledge, this paper is the first attempt to address this issue. The ground transfer resistances between the substation grounding grids and the buried pipelines are considered when we characterize their conductive coupling. Then, a nodal voltage analysis method is proposed to calculate the induced voltages and currents in the IPGS. The proposed circuit approach is verified by using the finite element analysis. In fact, this approach can provide more accurate results of induced voltages and currents in integrated systems compared to the classical models, which can help planners and operators in the energy sector develop comprehensive risk assessment and mitigation strategies for transformers, pipelines and other equipment.

The rest of this paper is organized as follows. Section II details the proposed geomagnetic induction model for the IPGS. Then, a simple case with a single power transmission line and a single buried pipeline is given in Section III, and the influences of IPGS characteristics and earth resistivity structures are discussed. In Section IV, the geomagnetic induction calculation is performed for a realistic large-scale IPGS test case. The induction results in the integrated systems calculated by the proposed model are compared with those by the classical models without considering the influence of earthing currents from the other network, and it clearly demonstrates the importance of considering the coupling between AC power grids and pipelines. Finally, Section V concludes this paper.

II. Geomagnetic Induction Model for IPGS

A. Equivalent Circuit of the IPGS Under GMD

Geomagnetic induction modeling in technological systems can usually be divided into two steps: a geophysical step and an engineering step [3]. In the geophysical step, the induced geoelectric field on the earth's surface is calculated based on the space current system and the earth resistivity structure [24].

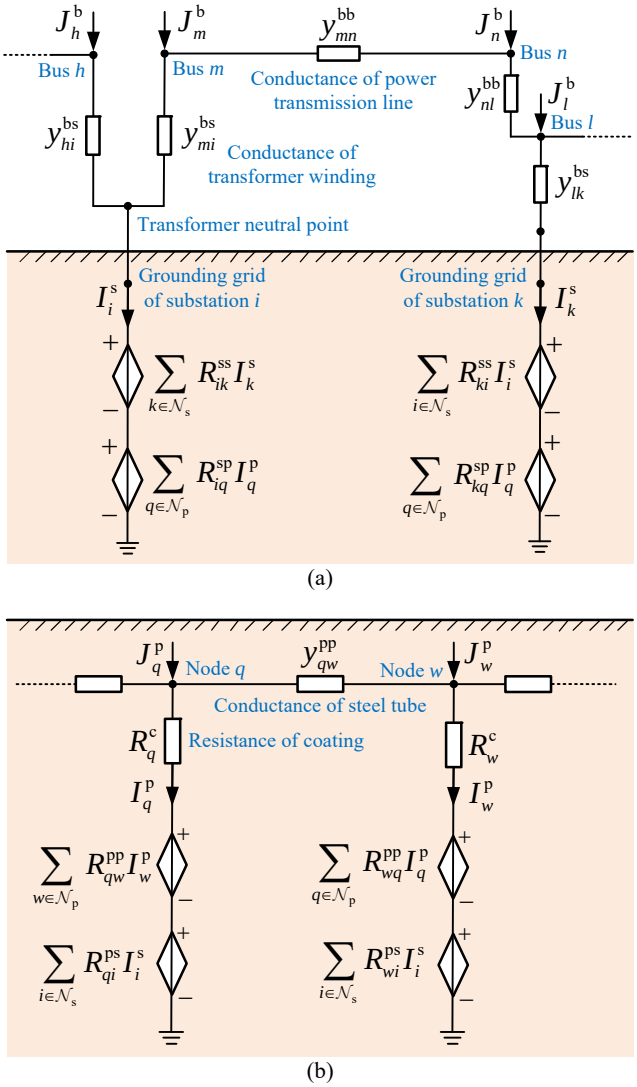

Fig. 1. Equivalent circuit of the IPGS for the geomagnetic induction analysis considering the conductive coupling through the earth. (a) Model of a power grid with multiple voltage levels. (b) Model of a buried pipe section of the gas pipeline network. The superscript of the variables refers to the type of the node ('b' for bus, 's' for substation grounding grid, and 'p' for pipe node), and the subscript refers to the index of the node, e.g. J_m is the current injection at node m, I_i is the earthing current of node i, y_{mn} is the admittance of the branch (m,n), R_{ik} is the ground transfer resistance between the grounded nodes i and k, and R_q^{c} is the coating resistance of the pipe node q.

In practice, it is difficult to obtain the accurate spatiotemporal distribution of the space current system. Thus, the geoelectric field $\mathbf{E}(\omega) = \begin{bmatrix} E_x(\omega) & E_y(\omega) \end{bmatrix}^\top$ can be calculated by using the measured geomagnetic field $\mathbf{B}(\omega) = \begin{bmatrix} B_x(\omega) & B_y(\omega) \end{bmatrix}^\top$ under the plane-wave assumption [2], [25], [26]:

$$\mathbf{E}(\omega) = \mathbf{K}(\omega) \cdot \mathbf{B}(\omega) \tag{1}$$

where $\mathbf{K}$ is the magnetotelluric transfer function, ω is the angular frequency, sub-x and sub-y refer to the components in the north and east directions.

Then in the engineering step, the low-frequency geoelectric field drives the induced currents in the IPGS, which can be calculated by utilizing the resistive circuit analysis. The equivalent circuit of Fig. 1 provides a simple illustrative IPGS

example involving a small portion of both the power grid and the gas pipeline network. We adopt current-controlled voltage sources to characterize the coupling of earthing currents of the substations and pipelines, and the derivation of the rest of the circuit can be found in [2], [15].

We consider a general power grid with multiple voltage levels, as shown in Fig. 1(a). The buses and substation grounding grids are regarded as nodes, and the node sets are denoted as $\mathcal{N}_{\rm b}$ and $\mathcal{N}_{\rm s}$, respectively. The GIC flow path inside the substation depends on the type and connection group of the transformers. Fig. 1(a) gives a typical example, where substation i contains a GY-GY transformer and substation k contains an auto-transformer. The transformer neutral point is connected to the substation grounding grid, and a capacitive or resistive GIC blocking device can be installed on this branch to mitigate the GIC.

The buried natural gas pipelines are continuously grounded through the insulation coating. Thus, we can discretize the pipes to establish a circuit model, as depicted in Fig. 1(b), and the resulting set of pipe nodes is denoted as $\mathcal{N}_{\rm p}$.

Thus, we can perform a nodal voltage analysis for the full-node set, including buses, substation grounding grids, and pipe nodes, which can be denoted as $\mathcal{N} = \mathcal{N}_{\rm b} \cup \mathcal{N}_{\rm s} \cup \mathcal{N}_{\rm p}$. The numbers of the three types of nodes are denoted as $n_{\rm b}$, $n_{\rm s}$, and $n_{\rm p}$, respectively.

The effect of the geoelectric field on the power grid can be modeled as a voltage source in the power line [2]. Then the voltage source can be converted into the current injections $\mathbf{J}_{\rm b}$ at buses with Norton equivalent system. The current injections at the substation grounding grids due to geoelectric fields are zero, since they are not directly connected to the long horizontal conductors. Thus, the nodal current injections in the power grid can be written in matrix form as

$$\mathbf{J}^{\rm b} = \mathbf{\Gamma}^{\rm b}\mathbf{E} \in \mathbb{R}^{n_{\rm b}\times 1}, \quad \mathbf{J}^{\rm s} = \mathbf{0} \in \mathbb{R}^{n_{\rm s}\times 1} \tag{2}$$

where $\mathbf{\Gamma}^{\rm b} \in \mathbb{R}^{n_{\rm b}\times 2}$ is the incident matrix for buses depending on power grid topology and power line resistances. In the illustrative example of Fig. 1(a), vector $\mathbf{J}^{\rm b}$ collects the current injections at buses h, m, n and l, yielding $\mathbf{J}^{\rm b} = [\ldots, J_h^{\rm b}, J_m^{\rm b}, J_n^{\rm b}, J_l^{\rm b}, \ldots]^\top$.

Similar to the buses, we can get the current injections at the pipe nodes

$$\mathbf{J}^{\rm p} = \mathbf{\Gamma}^{\rm p}\mathbf{E} \in \mathbb{R}^{n_{\rm p}\times 1} \tag{3}$$

where $\mathbf{\Gamma}^{\rm p} \in \mathbb{R}^{n_{\rm p}\times 2}$ is the incident matrix for pipelines. For the example of Fig. 1(b), vector $\mathbf{J}^{\rm p}$ collects the current injections at pipe nodes q and w, yielding $\mathbf{J}^{\rm p} = [\ldots, J_q^{\rm p}, J_w^{\rm p}, \ldots]^\top$.

The current injections due to the geoelectric field can produce GIC in the loop between the IPGS and the earth. The substation grounding grid and pipes are buried, and the earthing currents from them, $\mathbf{I}^{\rm s}$ and $\mathbf{I}^{\rm p}$, can produce a ground potential rise and thereby affect other grounded nodes. Such a conductive coupling is modeled as a current-controlled voltage source based on the ground transfer resistance, as depicted in Fig. 1. For instance, the grounding current $I_i^{\rm s}$ of the substation i results in an earth potential rise $R_{qi}^{\rm ps} I_i^{\rm s}$ near the pipe node q, where the transfer resistance $R_{qi}^{\rm ps}$ characterizes the coupling strength between these two nodes.

The ground transfer resistance between the grounded nodes depends on their spatial coordinates and the earth resistivity structures. The transfer resistance in the circuit model of IPGS, as shown in Fig. 1, can be applied to the cases of arbitrary earth structures. Appendix A details the methods for the calculation of the ground transfer resistance for different earth resistivity models, including uniform, 1D layered and 3D earth structures.

B. Nodal Voltage Analysis of the IPGS Under GMD

A nodal voltage analysis can be performed for the IPGS based on the equivalent circuit in Fig. 1. For the ungrounded bus node $m \in \mathcal{N}_{\rm b}$, according to the Kirchhoff's current law, we can obtain

$$\sum_{n\in\mathcal{N}_{\rm b}, n\neq m} y_{mn}^{\rm bb}(V_m^{\rm b} - V_n^{\rm b}) + \sum_{i\in\mathcal{N}_{\rm s}} y_{mi}^{\rm bs}(V_m^{\rm b} - V_i^{\rm s}) = J_m^{\rm b} \tag{4}$$

where $V_m^{\rm b}$ and $V_n^{\rm b}$ are the voltages of buses m and n, $V_i^{\rm s}$ is the voltage of substation grounding grid node i, $y_{mn}^{\rm bb}$is the admittance of the branch from bus m to bus n, $y_{mi}^{\rm bs}$ is the admittance of the branch from bus m to substation grounding grid node i, and $J_m^{\rm b}$ is the current injection at bus m.

Similarly, for the substation grounding grid node $i \in \mathcal{N}_{\rm s}$, one can get

$$\sum_{m\in\mathcal{N}_{\rm b}} y_{im}^{\rm sb}(V_i^{\rm s} - V_m^{\rm b}) + I_i^{\rm s} = 0 \tag{5}$$

where $I_i^{\rm s}$ is the current flowing into the earth from the substation grounding grid node i.

For the pipeline node $q \in \mathcal{N}_{\rm p}$, one can get

$$\sum_{w\in\mathcal{N}_{\rm p}, w\neq q} y_{qw}^{\rm pp}(V_q^{\rm p} - V_w^{\rm p}) + I_q^{\rm p} = J_q^{\rm p} \tag{6}$$

where $V_q^{\rm p}, V_w^{\rm p}$ are the voltages of the pipe nodes q and w, and $y_{qw}^{\rm pp}$ is the admittance of the steel tube between nodes q and w, $I_q^{\rm p}$ is the earthing current from the pipe node q, and $J_q^{\rm p}$ is the current injection at pipe node q.

In a nutshell, (4)-(6) for nodal voltages and earthing currents of the full nodes $\mathcal{N}$ can be written in matrix form as

$$\begin{bmatrix} \mathbf{Y}^{\rm bb} & \mathbf{Y}^{\rm bs} & \mathbf{0} \\ \mathbf{Y}^{\rm sb} & \mathbf{Y}^{\rm ss} & \mathbf{0} \\ \mathbf{0} & \mathbf{0} & \mathbf{Y}^{\rm pp} \end{bmatrix} \cdot \begin{bmatrix} \mathbf{V}^{\rm b} \\ \mathbf{V}^{\rm s} \\ \mathbf{V}^{\rm p} \end{bmatrix} + \begin{bmatrix} \mathbf{0} \\ \mathbf{I}^{\rm s} \\ \mathbf{I}^{\rm p} \end{bmatrix} = \begin{bmatrix} \mathbf{J}^{\rm b} \\ \mathbf{0} \\ \mathbf{J}^{\rm p} \end{bmatrix} \tag{7}$$

where the diagonal and off-diagonal entries of the blocks in the network admittance matrix $\mathbf{Y}$ are given by

$$\mathbf{Y}_{mm}^{\rm bb} = \sum_{n\in\mathcal{N}_{\rm b}, n\neq m} y_{mn}^{\rm bb} + \sum_{i\in\mathcal{N}_{\rm s}} y_{mi}^{\rm bs}, \quad \mathbf{Y}_{mn}^{\rm bb} = -y_{mn}^{\rm bb}, \tag{8a}$$

$$\mathbf{Y}_{ii}^{\rm ss} = \sum_{m\in\mathcal{N}_{\rm b}} y_{im}^{\rm sb}, \quad \mathbf{Y}_{ik}^{\rm ss} = 0, \tag{8b}$$

$$\mathbf{Y}_{qq}^{\rm pp} = \sum_{w\in\mathcal{N}_{\rm p}, w\neq q} y_{qw}^{\rm pp}, \quad \mathbf{Y}_{qw}^{\rm pp} = -y_{qw}^{\rm pp}, \tag{8c}$$

$$\mathbf{Y}_{mi}^{\rm bs} = \mathbf{Y}_{im}^{\rm sb} = -y_{mi}^{\rm bs} = -y_{im}^{\rm sb}. \tag{8d}$$

Furthermore, by considering the interaction of different grounding bodies through the ground transfer resistance in Appendix A, we can get a set of equations on the voltages

and earthing currents of the grounded nodes. The voltage of substation grounding grid i can be expressed as

$$V_i^{\mathrm{s}} = \sum_{k \in \mathcal{N}_{\mathrm{s}}} R_{ik}^{\mathrm{ss}} I_k^{\mathrm{s}} + \sum_{q \in \mathcal{N}_{\mathrm{p}}} R_{iq}^{\mathrm{sp}} I_q^{\mathrm{p}} \tag{9}$$

where R_{ii}^{ss} is the self-grounding resistance of the substation i, R_{ik}^{ss} is the mutual resistance between the substation grounding grid nodes i and k, and R_{iq}^{sp} is the mutual resistance between the substation grounding grid node i and the pipe node q.

Similarly, the voltage of the pipe node q can be expressed as

$$V_q^{\mathrm{p}} = R_q^{\mathrm{c}} I_q^{\mathrm{p}} + \sum_{w \in \mathcal{N}_{\mathrm{p}}} R_{qw}^{\mathrm{pp}} I_w^{\mathrm{p}} + \sum_{i \in \mathcal{N}_{\mathrm{s}}} R_{qi}^{\mathrm{ps}} I_i^{\mathrm{s}} \tag{10}$$

where R_q^{c} is the resistance of insulation coating of the pipe node q, and R_{qw}^{pp} is the mutual resistance between the pipe nodes q and w.

To sum up, the relationship between the nodal voltages and earthing currents (9)-(10) can be written in matrix form as

$$\begin{bmatrix} \mathbf{V}^{\mathrm{s}} \\ \mathbf{V}^{\mathrm{p}} \end{bmatrix} = \begin{bmatrix} \mathbf{R}^{\mathrm{ss}} & \mathbf{R}^{\mathrm{sp}} \\ \mathbf{R}^{\mathrm{ps}} & \mathbf{R}^{\mathrm{c}} + \mathbf{R}^{\mathrm{pp}} \end{bmatrix} \cdot \begin{bmatrix} \mathbf{I}^{\mathrm{s}} \\ \mathbf{I}^{\mathrm{p}} \end{bmatrix} \tag{11}$$

where $\mathbf{R}^{\mathrm{ss}}$, $\mathbf{R}^{\mathrm{sp}}$, $\mathbf{R}^{\mathrm{ps}}$, and $\mathbf{R}^{\mathrm{pp}}$ are ground transfer resistance matrices consisting of the self-grounding resistances and mutual resistances, and $\mathbf{R}^{\mathrm{c}}$ is a diagonal matrix of the coating resistance.

Then, equations (7) and (11) can be combined to solve for the induced voltages and currents. Two solution schemes are discussed in the next two subsections.

C. Solution Scheme 1 by Eliminating the Voltages of Grounded Nodes

If (11) is directly substituted into (7), then the final equations can be obtained by eliminating the voltages of the grounded nodes, as can be seen in (12) at the bottom of the page, where $\mathbb{I}_{n_{\mathrm{s}}} \in \mathbb{R}^{n_{\mathrm{s}} \times n_{\mathrm{s}}}$ and $\mathbb{I}_{n_{\mathrm{p}}} \in \mathbb{R}^{n_{\mathrm{p}} \times n_{\mathrm{p}}}$ are identity matrices. We can observe that the design matrix is asymmetric, so (12) can be solved based on LU factorization. The induced voltages and currents can be obtained by forward and backward substitution algorithms.

D. Solution Scheme 2 by Eliminating the Grounding Currents

In the second solution scheme, first we transform (11) into

$$\begin{bmatrix} \mathbf{I}^{\mathrm{s}} \\ \mathbf{I}^{\mathrm{p}} \end{bmatrix} = \begin{bmatrix} \mathbf{G}^{\mathrm{ss}} & \mathbf{G}^{\mathrm{sp}} \\ \mathbf{G}^{\mathrm{ps}} & \mathbf{G}^{\mathrm{pp}} \end{bmatrix} \cdot \begin{bmatrix} \mathbf{V}^{\mathrm{s}} \\ \mathbf{V}^{\mathrm{p}} \end{bmatrix} \tag{13}$$

where the ground transfer conductance matrices $\mathbf{G}^{\mathrm{ss}}$, $\mathbf{G}^{\mathrm{sp}}$, $\mathbf{G}^{\mathrm{ps}}$, and $\mathbf{G}^{\mathrm{pp}}$ are given as

$$\begin{bmatrix} \mathbf{G}^{\mathrm{ss}} & \mathbf{G}^{\mathrm{sp}} \\ \mathbf{G}^{\mathrm{ps}} & \mathbf{G}^{\mathrm{pp}} \end{bmatrix} = \begin{bmatrix} \mathbf{R}^{\mathrm{ss}} & \mathbf{R}^{\mathrm{sp}} \\ \mathbf{R}^{\mathrm{ps}} & \mathbf{R}^{\mathrm{c}} + \mathbf{R}^{\mathrm{pp}} \end{bmatrix}^{-1} \tag{14}$$

Substituting (13) into (7), we can obtain the nodal voltage equation by eliminating the earthing currents:

$$\begin{bmatrix} \mathbf{Y}^{\mathrm{bb}} & \mathbf{Y}^{\mathrm{bs}} & \mathbf{0} \\ \mathbf{Y}^{\mathrm{sb}} & \mathbf{Y}^{\mathrm{ss}} + \mathbf{G}^{\mathrm{ss}} & \mathbf{G}^{\mathrm{sp}} \\ \mathbf{0} & \mathbf{G}^{\mathrm{ps}} & \mathbf{Y}^{\mathrm{pp}} + \mathbf{G}^{\mathrm{pp}} \end{bmatrix} \cdot \begin{bmatrix} \mathbf{V}^{\mathrm{b}} \\ \mathbf{V}^{\mathrm{s}} \\ \mathbf{V}^{\mathrm{p}} \end{bmatrix} = \begin{bmatrix} \mathbf{J}^{\mathrm{b}} \\ \mathbf{0} \\ \mathbf{J}^{\mathrm{p}} \end{bmatrix} \tag{15}$$

The design matrix in (15) is symmetric positive definite, thus it can be solved by Cholesky factorization, which is more efficient than general LU factorization. In geomagnetic induction analysis, (15) usually needs to be solved repeatedly, taking into account the time-varying geoelectric field, changes in power grid topology, uncertain resistance parameters, etc. Thus, the solution scheme 2 is more computationally efficient than scheme 1.

As a special case, if we ignore the coupling between grounding bodies, i.e. all the mutual resistance entries are assumed to be zero, then (15) reduces to the classical nodal admittance matrix method.

Once the nodal voltages are solved, we can further obtain some auxiliary outputs of interest. For instance, the transformer effective GIC [6] are the weighted sum of the currents in the windings:

$$\mathbf{I}_{\mathrm{t}} = \mathbf{\Phi} \cdot \begin{bmatrix} \mathbf{V}^{\mathrm{b}} \\ \mathbf{V}^{\mathrm{s}} \end{bmatrix} \tag{16}$$

where $\mathbf{\Phi} \in \mathbb{R}^{n_{\mathrm{t}} \times (n_{\mathrm{b}} + n_{\mathrm{s}})}$ is the transformation matrix, and n_{t} is the number of transformers of interest.

In the pipeline networks, PSP refers to the voltage inside and outside the insulation coating, which can be calculated as

$$\mathbf{V}^{\text{p-soil}} = \mathbf{R}^{\mathrm{c}} \mathbf{I}^{\mathrm{p}} = \mathbf{R}^{\mathrm{c}} \left(\mathbf{G}^{\mathrm{ps}} \mathbf{V}^{\mathrm{s}} + \mathbf{G}^{\mathrm{pp}} \mathbf{V}^{\mathrm{p}} \right) \tag{17}$$

E. Procedures of the Induction Calculation for the IPGS

Fig. 2 summarizes the procedures of geomagnetic induction modeling in IPGS based on the nodal voltage analysis method. The inputs of the algorithm include: 1) the space current system or the surface geomagnetic field; 2) the earth resistivity structure; 3) the spatial coordinates, topology and resistance parameters of the IPGS. The outputs are the induced currents and voltages in the IPGS.

It can be seen that the earth resistivity structure plays a key role in the algorithm. It can affect both the nodal current injections and the ground transfer conductance matrix of the IPGS. Hence, accurate earth resistivity parameters are required for the geomagnetic induction calculation.

In this paper, the conductive coupling between the substation grounding grids and the buried pipelines are modeled by the transfer resistance in the circuit model of IPGS. And the proposed circuit approach is validated by using the finite element analysis in Appendix B.

$$\left[\begin{array}{c|c|c} \mathbf{Y}^{\mathrm{bb}} & \mathbf{Y}^{\mathrm{bs}}\mathbf{R}^{\mathrm{ss}} & \mathbf{Y}^{\mathrm{bs}}\mathbf{R}^{\mathrm{sp}} \\ \hline \mathbf{Y}^{\mathrm{sb}} & \mathbf{Y}^{\mathrm{ss}}\mathbf{R}^{\mathrm{ss}} + \mathbb{I}_{n_{\mathrm{s}}} & \mathbf{Y}^{\mathrm{ss}}\mathbf{R}^{\mathrm{sp}} \\ \hline \mathbf{0} & \mathbf{Y}^{\mathrm{pp}}\mathbf{R}^{\mathrm{ps}} & \mathbf{Y}^{\mathrm{pp}}\left(\mathbf{R}^{\mathrm{c}} + \mathbf{R}^{\mathrm{pp}}\right) + \mathbb{I}_{n_{\mathrm{p}}} \end{array}\right] \cdot \left[\begin{array}{c} \mathbf{V}^{\mathrm{b}} \\ \hline \mathbf{I}^{\mathrm{s}} \\ \hline \mathbf{I}^{\mathrm{p}} \end{array}\right] = \left[\begin{array}{c} \mathbf{J}^{\mathrm{b}} \\ \hline \mathbf{0} \\ \hline \mathbf{J}^{\mathrm{p}} \end{array}\right] \tag{12}$$

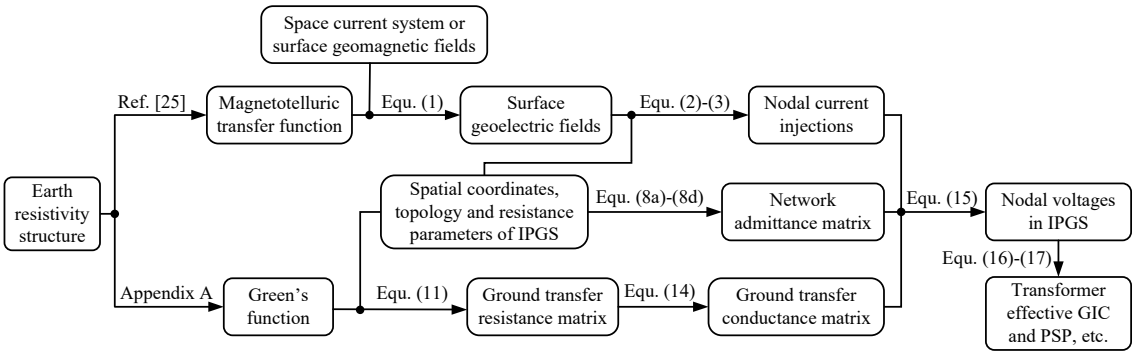

Fig. 2. Flow chart of geomagnetic induction algorithm for the IPGS.

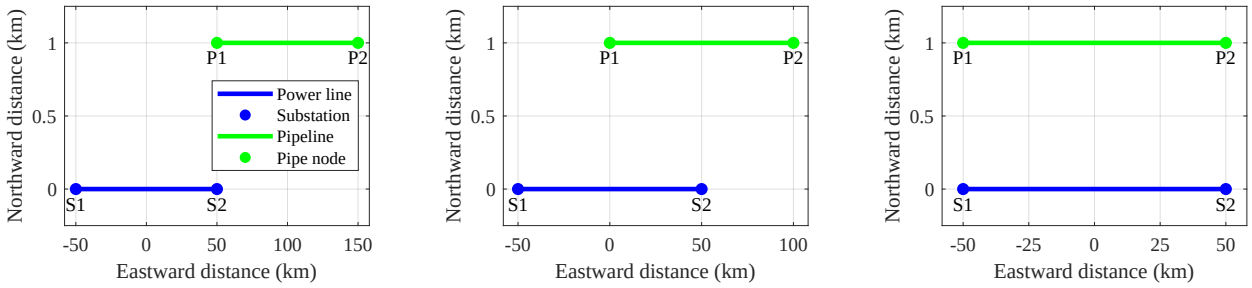

Fig. 3. Three typical spatial patterns of IPGS with single power line and single pipeline. (a) spatial pattern 1. (b) spatial pattern 2. (c) spatial pattern 3.

III. Simple IPGS Test Cases With Single Power Line and Single Pipeline

A. IPGS With Different Spatial Patterns

Let us start with a simple synthetic IPGS case with double-circuit power transmission lines, a single pipeline, two substations S1 and S2, two pipeline terminals P1 and P2. The default parameters for the power grid and pipeline are set as follows. The voltage level of the power grid is 750 kV. The length of the power line is 100 km, and the resistance per unit length of single-circuit line is 0.01205 Ω/km per phase. Each substation contains two auto-transformers, and the equivalent winding resistance of each transformer is 0.3852 Ω per phase, and the substation grounding resistance is 0.2 Ω [11]. The series impedance and parallel admittance of the pipeline are 0.005 Ω/km and 0.05 S/km, respectively [14]. The buried depth of the pipeline is 1.5 m, and both terminals of the pipe are electrically insulated. The power line is parallel to the pipeline in the east-west direction, and the minimum distance between the substation and the pipeline is 1 km.

In engineering practice, there are various spatial intersections between power grids and pipelines. Three typical spatial patterns are considered in the test cases, as shown in Fig. 3:

1) The east terminal of the power line is close to the west terminal of the pipeline, i.e. the substation S2 is close to the pipe node P1.
2) The east terminal of the power line is near the center of the pipeline.
3) The west terminal of the power line is near that of the pipeline, and so is the east terminal.

TABLE I
1D Layered Testing Resistivity Structure [23]

Layer	Thickness (m)	Resistivity (Ω·m)
1	6	70
2	25	120
3	60	90
4	300	220
5	500	500
6	3500	2500
7	13100	34385
8	17100	5324
9	97600	83095
10	∞	813

The IPGS cases are assumed to be located on a 1D horizontally layered Testing earth structure from [23], as shown in Table I. The resistivity of shallow soil can be inverted by electrical sounding methods, such as the four-electrode Wenner method [27], whereas the deep earth structure is obtained by magnetotelluric survey.

B. Results of Different Geomagnetic Induction Models

To illustrate the interaction of the power grid and pipelines in geomagnetic induction, we compare the results of three induction models for the IPGS test case in Fig. 3:

1) In the proposed induction model 1, the mutual resistances between all grounded nodes, including substation grounding grids and buried pipelines, are preserved.
2) In the classical induction model 2, the mutual resistances between all grounded nodes are neglected. This assump-

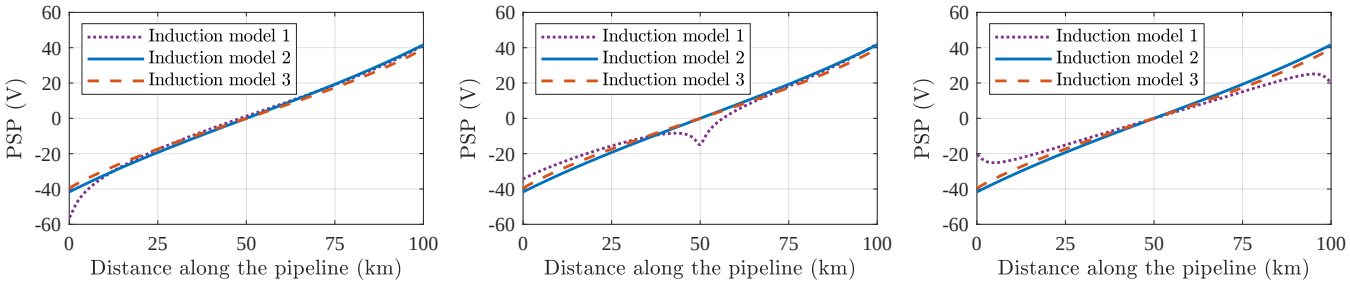

Fig. 4. Comparison of PSP along the pipeline P1-P2 obtained by three induction models. (a) PSP of spatial pattern 1. (b) PSP of spatial pattern 2. (c) PSP of spatial pattern 3. (Induction model 1: with all the mutual resistance in the IPGS. Induction model 2: without all mutual resistance in the IPGS. Induction model 3: with mutual resistance of the pipe nodes only)

tion is widely adopted by existing geomagnetic induction studies.

3) In the induction model 3, the mutual resistances between the substation grounding grid nodes and the mutual resistance between the pipeline nodes are preserved, whereas the mutual resistances between these two types of nodes are neglected.

The induction models 2 and 3 are used as references. For pipelines, the difference in the induction results of the induction models 2 and 3 represents the contribution of interaction between the pipe nodes, whereas the difference of the induction models 1 and 3 reveals the contribution of coupling from the substation grounding grid. The same goes for the power grid.

The PSP along the pipeline calculated by the three induction models are compared in Fig. 4. By comparing the PSP of induction models 2 and 3, it can be seen that ignoring the coupling between the pipe nodes could lead to a slight increase in the PSP amplitude. It means that the classical distributed source transmission line model [13] for pipelines can usually provide a more conservative estimate for PSP.

By comparing the PSP of induction models 1 and 3 in Fig. 4, we can see that the presence of the power grid greatly affects the PSP along the pipeline, whose charscteristics depend on the spatial pattern of IPGS:

1) For IPGS spatial pattern 1, the grounding current of substation S2 is in the opposite direction to the earthing current of pipe node P1. In this case, if the influence of the power grid is considered, the PSP of node P1 changes from -39.69 V to -56.06 V (41.24% increase in PSP amplitude).
2) For IPGS spatial pattern 2, the earthing current in the middle of the pipeline is zero when the power grid does not exist. However, in the presence of the power grid, a PSP spike with an amplitude of -14.92 V is generated near the middle of the pipeline. The substation grounding GIC may cause significant changes in the induction results in nearby pipeline segments.
3) For IPGS spatial pattern 3, the grounding current of substation S2 is in the same direction as the earthing current of pipe node P1. In this case, the PSP of node P1 changes from -39.69 V to -21.08 V in the presence of the power grid (46.89% reduction in PSP amplitude).

TABLE II
SUBSTATION GROUNDING GIC IN THE CASES OF DIFFERENT SPATIAL PATTERNS OF THE IPGS

Spatial pattern of the IPGS	GIC of S2 (A)	Increment*
1	150.06	2.53 %
2	146.33	-0.02 %
3	140.98	-3.68 %

* GIC calculated by the induction model 3 without considering the pipeline, 146.36 A, is used as the base value.

In addition, the GIC in the power grid is also calculated by using three induction models. The grounding GIC of substation S2 obtained by induction models 2 and 3 are 137.13 A and 146.36 A, respectively. It means that ignoring the conductive coupling between the substation grounding grids could lead to an underestimate of the GIC by 6.73%.

A comparison of the results of induction models 1 and 3 characterizing the contribution of the pipeline is shown in Table II. The GIC variation mainly depends on the direction and magnitude of the earthing current in the pipeline near the substation. Overall, the influence of the power grid on the pipeline in geomagnetic induction is greater than that of the pipeline on the power grid.

C. Influence of Pipeline Parameter

In addition to the spatial pattern, the resistance parameters of the IPGS may also have a large impact on the induction results. For instance, the parallel admittance of pipelines depends on the material and thickness of the insulation coating. The insulation performance of the coating could degrade with age in service, and leakage points may even appear.

A typical range of parallel admittance, 0.05-0.25 S/km, from [14] is chosen to analyze its influence on the induction results of the IPGS in Fig. 3(a). The normalized metrics, including percentage increment in PSP amplitude at pipe node P1 due to the power grid and the percentage increment in GIC amplitude at substation S2 due to the pipeline, are adopted to quantify the strength of the coupling between the power grid and the pipeline. It can be seen from Fig. 5 that with the increase of the parallel admittance of the pipeline, the coupling between

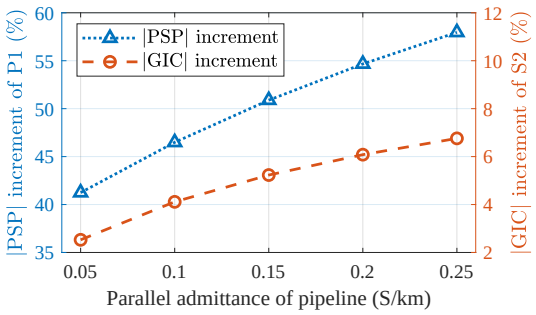

Fig. 5. The increment of the PSP amplitude of the pipe node P1 and the increment of the GIC amplitude of the substation S2 with respect to the parallel admittance of the pipeline.

TABLE III
SUBSTATION GROUNDING GIC IN THE CASES OF DIFFERENT GROUNDING MODES OF PIPE NODES

Grounding mode of pipe nodes	GIC of S2 (A)	Increment*
P1 insulated and P2 insulated	150.06	2.53 %
P1 insulated and P2 grounded	151.16	3.28 %
P1 grounded and P2 insulated	161.68	10.47 %
P1 grounded and P2 grounded	165.00	12.74 %

* GIC calculated by the induction model 3 without considering the pipeline, 146.36 A, is used as the base value.

the power grid and the pipeline is stronger due to the increase of the earthing currents of the pipeline.

In the above analysis, both terminals P1 and P2 of the pipeline are assumed to be electrically insulated. In engineering practice, additional grounding devices may be added to the pipe nodes. Thus, the influence of different grounding modes of pipe terminals on the induction results are analyzed in Table III. The grounding resistance of the pipe terminal is set to 0.5 Ω, which is chosen from its typical range [28]. It can be seen that if the pipe node P1 is grounded, the GIC in the power grid may increase significantly, which is mainly contributed by the earthing current concentrated at the node P1.

D. Influence of Earth Resistivity Structures

The resistivity structure of different geological zones varies greatly, especially in the shallow earth. Thus, we analyze the influence of four different earth structures on the geomagnetic induction. The variation of earth resistivity with depth is shown in Fig. 6 and the original data can be found in [10], [23]. The Testing, Guangdong, and Hubei models are 1D horizontally stratified. In addition, a uniform earth with 1000 Ω·m resistivity is considered, which is widely used in engineering standards to provide an estimate of the geoelectric field in the absence of knowledge about the geological structure [29].

Correspondingly, the ground transfer resistances of the four earth structures with respect to the horizontal distance are compared in Fig. 7. As the horizontal distance increases, the transfer resistance of the uniform earth decreases rapidly, whereas the transfer resistance of the Testing and Guangdong models decreases relatively slowly. This is mainly due to the presence of high resistivity layers in the deep earth for these two structures. In addition, the transfer resistance of the Hubei model is generally much smaller than the other three due to its overall lower earth resistivity.

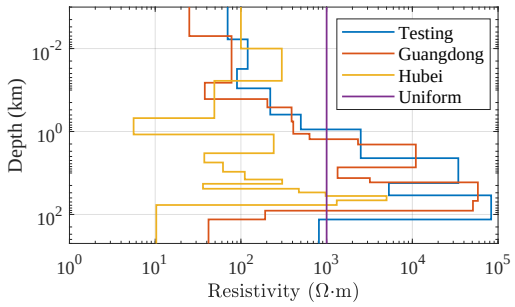

Fig. 6. Profiles of four typical earth resistivity structures.

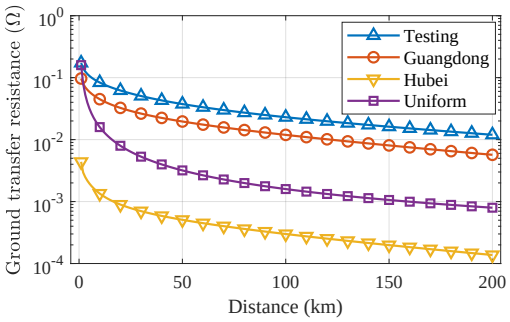

Fig. 7. The ground transfer resistance of the four earth resistivity structures with respect to the horizontal distance from the source point to the field point on the earth surface.

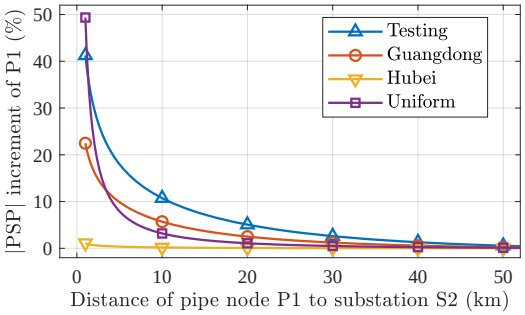

Fig. 8. The percentage increment of the PSP amplitude of the pipe node P1 in the cases of different earth resistivity structures.

Then, for IPGS with spatial pattern 1 in Fig. 3(a), the influence of the shortest distance from the substation to the pipeline on the induction is discussed. The output of interest is the percentage increment of the PSP amplitude of pipe node P1 due to the power grid, as shown in Fig. 8. It can be seen that when the distance from the substation S2 to the pipe node P1 is 1 km, the increment of PSP amplitude at node P1 of the uniform earth is higher than that of the three layered earth models. With the increase of the distance, the change of PSP decreases rapidly in the case of uniform earth, whereas the Testing and Guangdong earth models correspond to a larger effective coupling distance between the power grid and the pipeline. Hence, the detailed resistivity structure is required when designing the safe distance between the power grid and the pipeline for GMD in the IPGS planning stage.

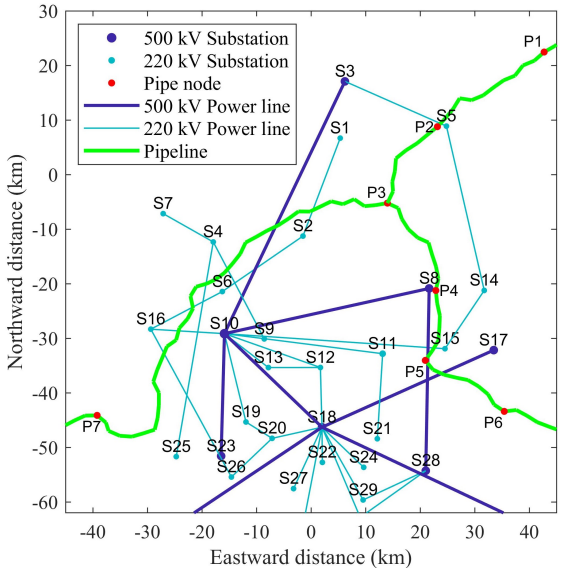

Fig. 9. Spatial location and topology of the IPGS test case [23].

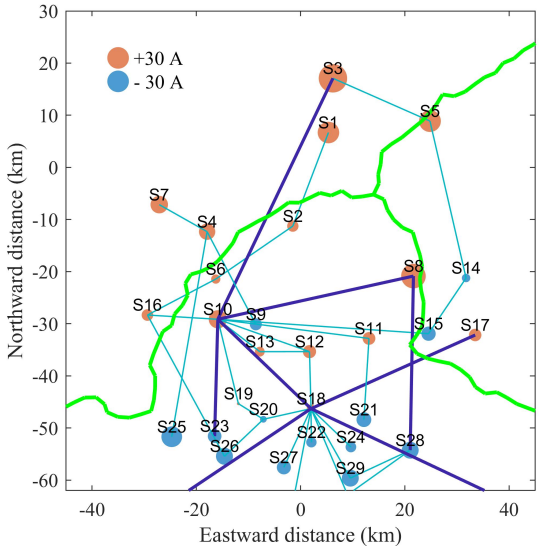

Fig. 10. Snapshot of the substation grounding GIC considering pipelines in the case of 1 V/km northward geoelectric field.

IV. A Realistic Large-Scale IPGS Case

In this section, a realistic IPGS case from [23] is adopted for geomagnetic induction analysis. The spatial coordinates and topology of the power grid and pipelines are shown in Fig. 9. There is an insulating joint at the pipe node P5, thus the pipeline P4-P5 and the pipeline P5-P6 are electrically insulated. The IPGS is located on the Testing earth resistivity structure in Table I.

Geomagnetic induction in the IPGS is analyzed in the case of 1 V/km northward geoelectric field. The spatial distribution of GIC in the power grid considering the influence of pipelines is shown in Fig. 10. Large grounding GIC can be found at substations S5, S8 and S15 near the pipeline. The substation grounding GIC with and without the pipelines are compared in Fig. 11. The GIC increment of each substation with respects to its shortest distance to the pipeline is shown in Fig. 12. The GIC amplitudes of substations S6 and S16 increase by more than 20% due to the pipeline, whereas the relative variation of GIC amplitude at most substations are basically within 10%.

Fig. 13 shows the PSP along the pipeline P1-P5 with 1 V/km northward geoelectric field. Under the influence of the power grid, the PSP amplitude of node P2 increases by 69.07%, while the PSP amplitude of node P5 decreases by 7.00%. It mainly depends on the size and orientation of the substation grounding GIC adjacent to the pipe nodes.

Also, PSP along the pipeline P1-P5 in the case of 1 V/km eastward geoelectric field is given in Fig. 14. The polarities of the PSP at node P4 and P5 are even reversed due to the power grid. Overall, the contribution from the power grid to the PSP along the pipeline differs significantly in the cases of northward and eastward geoelectric fields.

In addition, we evaluated the induction results in the IPGS during the historical GMD event on July 15-16, 2000. Fig. 15 shows the geomagnetic variations at Beijing Ming Tombs (BMT) observatory from SuperMAG. Fig. 16 compares the PSP waveforms of the pipe node P2 with and without consideration of the power grid, which shows that ignoring the power grid may lead to an underestimation of the PSP level.

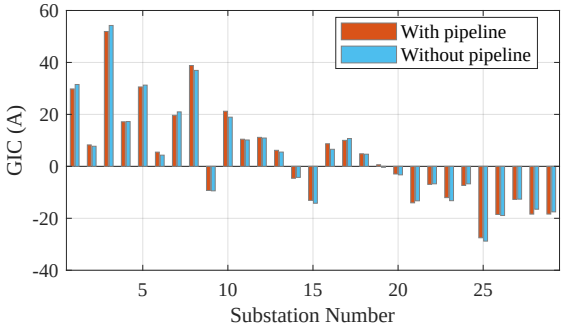

Fig. 11. Substation grounding GIC with and without pipelines.

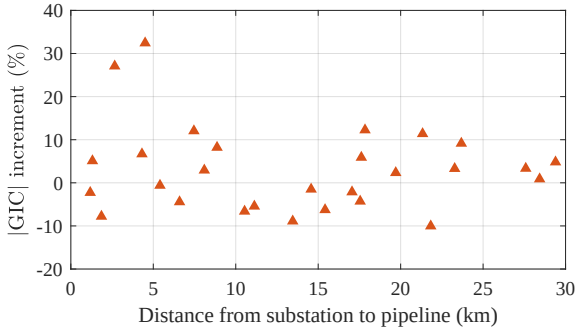

Fig. 12. The GIC increment of each substation due to the pipelines with respect to its distance to the pipeline.

V. Conclusion and Future Work

This paper proposes a geomagnetic induction model for the IPGS by considering the interaction of the power grids and buried pipelines. The proposed model can assist the energy sector in assessing the GMD risks of the IPGS in a more

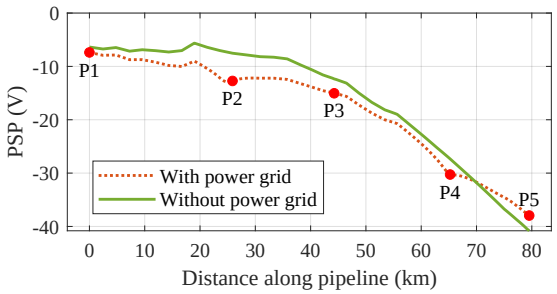

Fig. 13. PSP along the pipeline P1-P5 with and without the power grid in the case of 1 V/km northward geoelectric field.

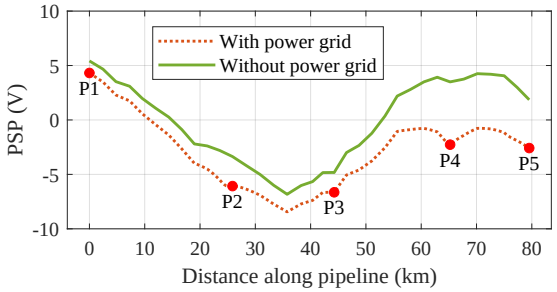

Fig. 14. PSP along the pipeline P1-P5 with and without the power grid in the case of 1 V/km eastward geoelectric field.

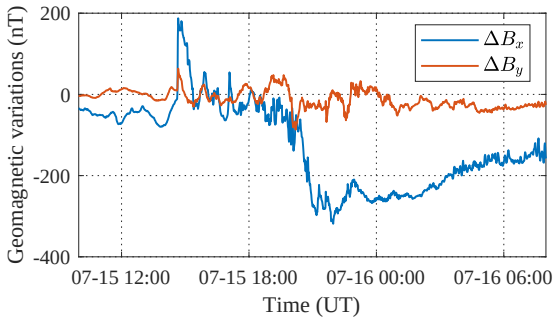

Fig. 15. Geomagnetic variations at BMT observatory during the historical GMD event on July 15-16, 2000.

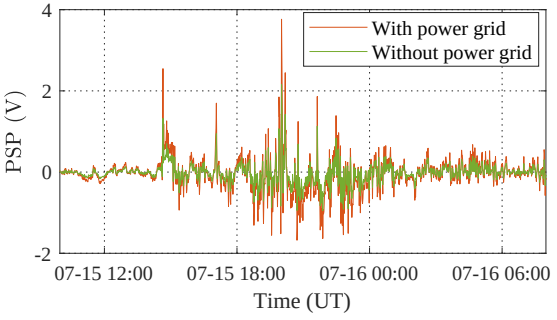

Fig. 16. Comparison of the PSP waveforms at the pipe node P2 with and without power grid during the GMD event on July 15-16, 2000.

comprehensive manner, thus developing more effective and targeted mitigation measures.

Several IPGS test cases are used to illustrate the contribution of the conductive coupling through the earth to the induction results. The results show that for the geomagnetic induction

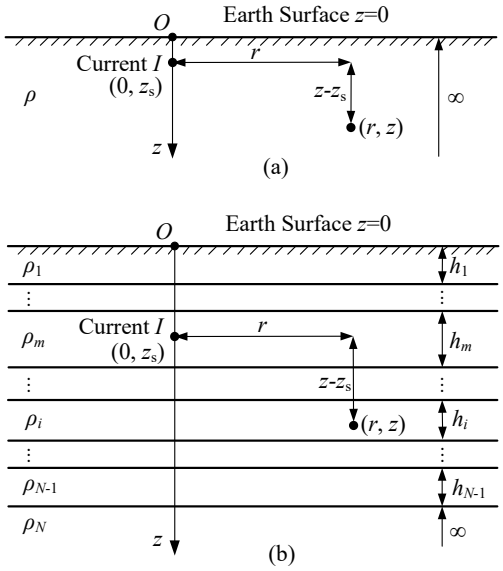

Fig. 17. Schematic diagram of earth resistivity structures. (a) Uniform earth. (b) 1D Horizontally layered earth. The point current source I is added for Green's function analysis.

analysis in infrastructure networks, it is necessary to take into account the influence of other adjacent conductor systems.

The spatial pattern of the IPGS, including the location of power lines, substations, and pipelines, could affect the increase or decrease trend of PSP and GIC. The resistance parameters of the power grid and pipelines may affect the strength of the coupling. In addition, the effective coupling distance between the substations and the pipelines depends on the earth resistivity structure.

Future work includes the geomagnetic induction modeling for the IPGS located on the complex earth structures with 3D heterogeneous resistivity, as well as the GMD risk assessment considering functional dependencies in the IPGS.

APPENDIX A
GREEN'S FUNCTION OF A EARTH MODEL FOR GROUND TRANSFER RESISTANCE CALCULATION

The conductive coupling in the IPGS during GMD can be modeled through the ground transfer resistance as in Fig. 1 and equations (9)-(10). In this appendix, we discuss its calculation methods for different earth models, including uniform, 1D layered and 3D structures.

Green's function is the basis for the calculation of transfer resistance, which refers to the ground potential V generated by a unit point current source I [30]. If the distance between two grounding bodies is much larger than their size, the earthing current can be regarded as a point current source for ground transfer resistance calculations. Thus, the ratio of V/I can be defined as the ground transfer resistance between the source and field points. Otherwise, it is required to consider the detailed current distribution inside the grounding body to obtain the earth potential rise.

The Green's function depends on the earth resistivity structure. It can be solved analytically for the uniform earth and the 1D layered earth, as depicted in Fig. 17. These two simplified

resistivity structures are widely used in GMD studies [2], and they are the special cases for the earth in Fig. 1.

For a homogeneous soil model with resistivity ρ in Fig. 17(a), the point current source I is assumed to be at the depth z_{s}. We build a cylindrical coordinate system with the point directly above it situated on the earth surface as the origin, i.e. the earth surface is set to $z = 0$. Thus, the potential at the coordinate (r, z) in the soil can be calculated analytically via the method of images as [31]

$$V(r,z) = \frac{\rho I}{4\pi} \cdot \left[\frac{1}{\sqrt{r^2 + (z - z_{\mathrm{s}})^2}} + \frac{1}{\sqrt{r^2 + (z + z_{\mathrm{s}})^2}} \right] \tag{18}$$

where r is the horizontal distance between the source and field point, and z is the depth of the field point.

This simple uniform earth can provide us some valuable insights. The interaction between the ground bodies is stronger as the resistivity increases and the distance decreases.

For a layered earth model in Fig. 17(b), the point current source I is assumed to be located in the m-th layer. According to the potential equation and boundary conditions in the soil, the potential at the coordinate (r, z) in the i-th layer can be deduced as [30]

$$\begin{aligned} V_i^m(r,z) = {} & \frac{\rho_m I}{4\pi} \int_0^\infty \delta(m-i)\, e^{-\lambda|z-z_{\mathrm{s}}|} J_0(\lambda r)\, \mathrm{d}\lambda \\ & + \frac{\rho_i I}{4\pi} \int_0^\infty \varphi(\lambda)\, e^{-\lambda(z-z_{\mathrm{s}})} J_0(\lambda r)\, \mathrm{d}\lambda \\ & + \frac{\rho_i I}{4\pi} \int_0^\infty \psi(\lambda)\, e^{\lambda(z-z_{\mathrm{s}})} J_0(\lambda r)\, \mathrm{d}\lambda \end{aligned} \tag{19}$$

where $\delta(0) = 1$ and $\delta(m-i) = 0$ for $m \neq i$; $J_0(\cdot)$ is the zero-order Bessel's function of the first kind; $\varphi(\lambda)$ and $\psi(\lambda)$ are kernel functions that depend on the soil resistivity parameters and depth of the source point [32].

Substation grounding grids and natural gas pipelines are typically buried at a depth of several meters. Thus, if the source and field points of interest are both in the top layer of soil, the general solution for the potential in (19) can be rewritten as [33]

$$\begin{aligned} V(r,z) = \frac{\rho_1 I}{4\pi} \Bigg\{ & \frac{1}{\sqrt{r^2 + (z - z_{\mathrm{s}})^2}} + \frac{1}{\sqrt{r^2 + (z + z_{\mathrm{s}})^2}} \\ & + \int_0^\infty f(\lambda) \begin{bmatrix} e^{-\lambda(z-z_{\mathrm{s}})} + e^{-\lambda(z+z_{\mathrm{s}})} \\ + e^{\lambda(z-z_{\mathrm{s}})} + e^{\lambda(z+z_{\mathrm{s}})} \end{bmatrix} J_0(\lambda r)\, \mathrm{d}\lambda \Bigg\} \end{aligned} \tag{20}$$

where $f(\lambda)$ depends on the earth resistivity parameters, which can be obtained in a recursive manner from the bottom layer to the top layer [33].

Note that there is an improper integral in the potential solution (20) with an infinite upper limit and an oscillatory kernel function. Thus, the numerical integration method is computationally expensive. As an alternative, the complex image method [27] can be used to efficiently obtain approximate solutions.

For the earth structure with 3D complex resistivity distributions, there is usually no analytical solution for the potential distribution. Instead, it can be solved by numerical approaches such as finite element or boundary element analysis. According to the current conservation law, the governing equations can be written as

$$\nabla \cdot \mathbf{J}_{\mathrm{c}} = 0 \tag{21}$$

$$\mathbf{J}_{\mathrm{c}} = \sigma \mathbf{E} + \mathbf{J}_{\mathrm{e}} \tag{22}$$

$$\mathbf{E} = -\nabla V \tag{23}$$

where $\mathbf{J}_{\mathrm{c}}$ is the conduction current density, $\mathbf{E}$ is the electric field intensity, $\mathbf{J}_{\mathrm{e}}$ is the externally generated current density, σ is the conductivity, and V is the electrical potential.

And the earth surface is subject to the boundary condition of electrical insulation:

$$\mathbf{n} \cdot \mathbf{J}_{\mathrm{c}} = 0 \tag{24}$$

where $\mathbf{n}$ is the normal vector of the earth's surface.

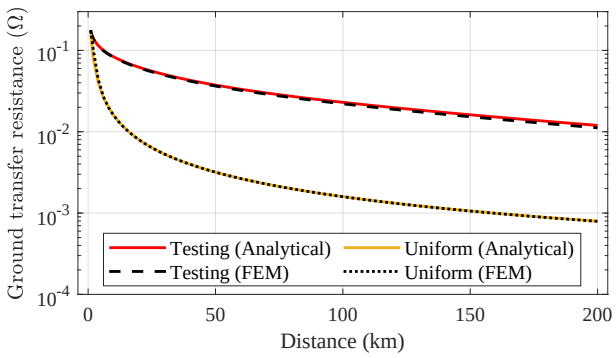

Fig. 18. Comparison of the ground transfer resistances of the uniform 1000 Ω·m earth and the 1D layered Testing earth obtained by analytical solution and FEM.

APPENDIX B
MODEL VALIDATION VIA FINITE ELEMENT ANALYSIS

In this appendix, the proposed circuit model of the IPGS based on the ground transfer resistance is verified by using the finite element method (FEM). The electrical potential distribution is solved using the Electric Currents interface under the AC/DC module of COMSOL Multiphysics software, which is based on the finite element solution for (21)-(24).

First, we establish 3D models for the uniform 1000 Ω·m earth model and the 1D layered Testing earth structure in Table I in COMSOL software, respectively. A unit point current is applied to the earth surface. The ground transfer resistance results at the earth surface obtained by the FEM are presented in Fig. 18, which are in good agreement with the analytical solutions from (18) and (20). The established finite element model can be further used to analyze the earth with 3D complex resistivity distribution.

Then, we built a comprehensive finite element model that includes the uniform earth and the pipeline, and the schematic diagram is shown in Fig. 19(a). A 0.001 Hz and 10 A point current is injected at the origin to represent the substation grounding current. The horizontal distance from the current source to the center of the buried pipeline is 15 m. The pipeline is along the y-axis and its two ends are insulated. The length of the pipeline is 100 m, and its buried depth is 1.5 m. The

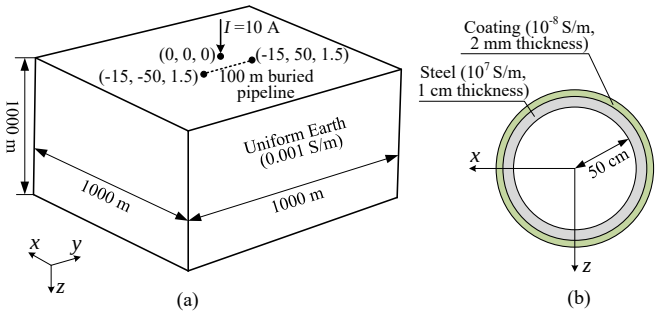

Fig. 19. The finite element model that involves the uniform earth, a buried pipeline, and one point current excitation. (a) Schematic diagram of the whole model. (b) Cross section of the pipeline.

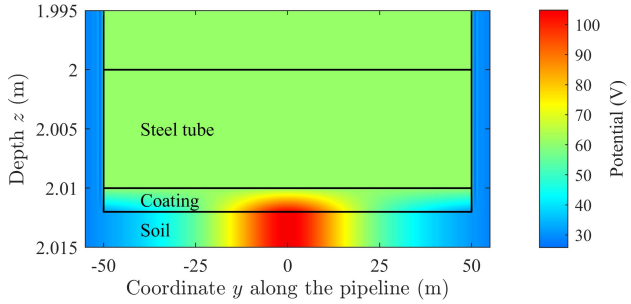

Fig. 20. Potential distribution in the yOz plane of the pipeline obtained by FEM.

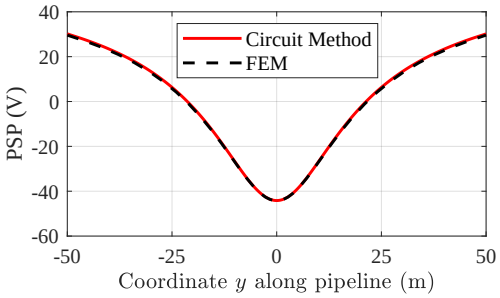

Fig. 21. Comparison of the PSP results along the pipeline obtained by circuit method and FEM.

cross section of the pipe is shown in Fig. 19(b), where the conductivity and thickness of the steel tube and coating are taken from [14].

The potential distribution on the yOz plane of the pipeline calculated by the FEM is shown in Fig. 20. It can be observed that there is a large potential difference between the steel side and the soil side of the coating, which illustrates the influence of the earthing GIC from the power grid on the pipe. The PSP results of the FEM are compared with those of the proposed circuit method in Fig. 21. The results of the two methods are highly consistent, which indicates that the circuit method adopted in this paper is reasonable to analyze the conductive coupling in IPGS during GMD.

ACKNOWLEDGMENT

For the geomagnetic data at BMT observatory used in this paper, the authors gratefully acknowledge the SuperMAG ground magnetometer data (http://supermag.jhuapl.edu/info/?page=acknowledgement). The work was supported by the HPC platform at Xi'an Jiaotong University.

REFERENCES

[1] A. Pulkkinen *et al.*, "Geomagnetically induced currents: Science, engineering, and applications readiness," *Space Weather*, vol. 15, no. 7, pp. 828–856, 2017.
[2] D. Boteler and R. Pirjola, "Modeling geomagnetically induced currents," *Space Weather*, vol. 15, no. 1, pp. 258–276, 2017.
[3] R. Pirjola, "Geomagnetically induced currents during magnetic storms," *IEEE Trans. Plasma Sci.*, vol. 28, no. 6, pp. 1867–1873, 2000.
[4] M. Lehtinen and R. J. Pirjola, "Currents produced in earthed conductor networks by geomagnetically-induced electric fields," *Ann. Geophys.*, vol. 3, pp. 479–484, 1985.
[5] D. H. Boteler and R. J. Pirjola, "Comparison of methods for modelling geomagnetically induced currents," *Ann. Geophys.*, vol. 32, no. 9, pp. 1177–1187, 2014.
[6] T. J. Overbye, K. S. Shetye, T. R. Hutchins, Q. Qiu, and J. D. Weber, "Power grid sensitivity analysis of geomagnetically induced currents," *IEEE Trans. Power Syst.*, vol. 28, no. 4, pp. 4821–4828, 2013.
[7] S. Marsal *et al.*, "A new standalone tool for DC-equivalent network generation and GIC calculation in power grids with multiple voltage levels," *Space Weather*, vol. 20, no. 3, p. e2021SW002984, 2022.
[8] M.-z. Liu, Y.-z. Xie, Y.-f. Yang, R. Trinchero, and I. S. Stievano, "Reduced nodal admittance matrix method for probabilistic GIC analysis in power grids," *IEEE Trans. Power Syst.*, pp. 1–4, 2023.
[9] R. Pirjola, "Effects of interactions between stations on the calculation of geomagnetically induced currents in an electric power transmission system," *Earth, Planets and Space*, vol. 60, no. 7, pp. 743–751, 2008.
[10] Z. Pan, L. Zhang, X. Wang, H. Yao, L. Zhu, Y. Liu, and X. Wen, "HVDC ground return current modeling in AC systems considering mutual resistances," *IEEE Trans. Power Del.*, vol. 31, no. 1, pp. 165–173, 2015.
[11] Q. Liu, "Study on the rules of geomagnetically induced currents in power grid based on uncertainty quantification method," Ph.D. dissertation, Xi'an Jiaotong University, Xi'an, China, 2020.
[12] Y.-h. Chen, Y.-z. Xie, M.-z. Liu, Z.-y. Wang, Q. Liu, and A.-c. Qiu, "Geomagnetically induced current calculation of high voltage power system with long transmission lines using Kriging method," *IEEE Trans. Power Del.*, vol. 37, no. 1, pp. 650–657, 2022.
[13] D. Boteler and M. Cookson, "Telluric currents and their effects on pipelines in the cook strait region of New-Zealand," *Mater. Perform.*, vol. 25, no. 3, pp. 27–32, 1986.
[14] A. Pulkkinen, R. Pirjola, D. Boteler, A. Viljanen, and I. Yegorov, "Modelling of space weather effects on pipelines," *J. Appl. Geophys.*, vol. 48, no. 4, pp. 233–256, 2001.
[15] D. Boteler, "A new versatile method for modelling geomagnetic induction in pipelines," *Geophys. J. Int.*, vol. 193, no. 1, pp. 98–109, 2013.
[16] M.-Z. Liu, Y.-Z. Xie, N. Dong, Z.-Y. Wang, and Y.-F. Yang, "Numerical analysis of nonuniform geoelectric field impacts on geomagnetic induction in pipeline networks," *IEEE Trans. Electromagn. Compat.*, vol. 64, no. 4, pp. 999–1009, 2022.
[17] L. Trichtchenko and D. H. Boteler, "Coupling between power systems and pipelines during geomagnetic disturbances," Geological Survey of Canada, Tech. Rep. Open File 7453, 2013.
[18] Z. Zeng, T. Ding, Y. Xu, Y. Yang, and Z. Dong, "Reliability evaluation for integrated power-gas systems with power-to-gas and gas storages," *IEEE Trans. Power Syst.*, vol. 35, no. 1, pp. 571–583, 2020.
[19] F. Dawalibi and R. Southey, "Analysis of electrical interference from power lines to gas pipelines. II. parametric analysis," *IEEE Trans. Power Del.*, vol. 5, no. 1, pp. 415–421, 1990.
[20] J. Yong, B. Xia, H. Yong, W. Xu, A. B. Nassif, and T. C. Hartman, "Harmonic voltage induction on pipelines: Measurement results and methods of assessment," *IEEE Trans. Power Del.*, vol. 33, no. 5, pp. 2170–2179, 2018.
[21] D. Boteler, C. A. Charalambous, and K. Lax, "New insights into calculations of AC interference at fundamental and harmonic frequencies taking account of the phase relationships of the currents," *IEEE Trans. Power Del.*, vol. 37, no. 2, pp. 851–859, 2022.
[22] A. Dimitriou and C. A. Charalambous, "Interpreting coating stress voltages on underground gas pipelines due to lightning strikes on adjacent power lines," in *2018 34th International Conference on Lightning Protection (ICLP)*, 2018, pp. 1–7.

[23] B. Zhang, F. Cao, R. Zeng, J. He, X. Meng, Y. Liao, and R. Li, "DC current distribution in both AC power grids and pipelines near HVDC grounding electrode considering their interaction," *IEEE Trans. Power Del.*, vol. 34, no. 6, pp. 2240–2247, Dec. 2019.
[24] K. Zheng, R. J. Pirjola, D. H. Boteler, and L.-g. Liu, "Geoelectric fields due to small-scale and large-scale source currents," *IEEE Trans. Power Del.*, vol. 28, no. 1, pp. 442–449, Jan. 2013.
[25] L. Marti, A. Rezaei-Zare, and D. Boteler, "Calculation of induced electric field during a geomagnetic storm using recursive convolution," *IEEE Trans. Power Del.*, vol. 29, no. 2, pp. 802–807, Apr. 2014.
[26] R. Sun and C. Balch, "Comparison between 1-D and 3-D geoelectric field methods to calculate geomagnetically induced currents: A case study," *IEEE Trans. Power Del.*, vol. 34, no. 6, pp. 2163–2172, Dec. 2019.
[27] B. Zhang, X. Cui, L. Li, and J. He, "Parameter estimation of horizontal multilayer earth by complex image method," *IEEE Trans. Power Del.*, vol. 20, no. 2, pp. 1394–1401, 2005.
[28] Z. Liu, B. Li, J. Zou, and C. Liu, "Research on calculation method of electromagnetic influence on buried metal pipeline networks due to HVDC grounding electrode current," *Power System Technology*, vol. 45, no. 4, pp. 1613 – 1617, 2021.
[29] R. H.-W. Lee, K. S. Shetye, A. B. Birchfield, and T. J. Overbye, "Using detailed ground modeling to evaluate electric grid impacts of late-time high-altitude electromagnetic pulses (E3 HEMP)," *IEEE Trans. Power Syst.*, vol. 34, no. 2, pp. 1549–1557, 2019.
[30] W. Li, Z. Pan, H. Lu, X. Chen, L. Zhang, and X. Wen, "Influence of deep earth resistivity on HVDC ground-return currents distribution," *IEEE Trans. Power Del.*, vol. 32, no. 4, pp. 1844–1851, 2017.
[31] R. Zeng, J. He, and B. Zhang, *Methodology and technology for power system grounding*. John Wiley & Sons, 2012.
[32] T. Takahashi and T. Kawase, "Calculation of earth resistance for a deep-driven rod in a multi-layer earth structure," *IEEE Trans. Power Del.*, vol. 6, no. 2, pp. 608–614, 1991.
[33] B. Zhang, R. Zeng, J. He, J. Zhao, X. Li, Q. Wang, and X. Cui, "Numerical analysis of potential distribution between ground electrodes of HVDC system considering the effect of deep earth layers," *IET Gener. Transm. Distrib.*, vol. 2, no. 2, pp. 185–191, 2008.

Min-zhou Liu (Graduate Student Member, IEEE) was born in Hebei, China, in 1995. He received the B.S. degree in electrical engineering from Xi'an Jiaotong University, Xi'an, China, in 2017. He is currently pursing the Ph.D. degree in electrical engineering under the double degree program jointly supported by Xi'an Jiaotong University and Politecnico di Torino, Turin, Italy. His current research interests include power system risk assessment, complex network, and electromagnetic effects.

Yan-zhao Xie (Senior Member, IEEE) received the Ph.D. degree in electrical engineering from Tsinghua University, Beijing, China, in 2005. He is currently a Professor with the School of Electrical Engineering, Xi'an Jiaotong University, Xi'an, China. Since 2016, he has been the Director of the National Center for International Research on Transient Electromagnetics and Applications (TEA). His research interests include electromagnetic compatibility, electromagnetic transients in power system, and high-power electromagnetics.

Yu-hao Chen was born in Shaanxi, China, in 1993. He received the B.Sc. and Ph.D. degrees in electrical engineering from Xi'an Jiaotong University, Xi'an, China, in 2015 and 2021, respectively. He is currently an Assistant Professor with the School of Electrical Engineering, Xi'an Jiaotong University. His research interests include effect evaluation of high-power electromagnetics and geomagnetic storm.

Riccardo Trinchero (Member, IEEE) received the M.Sc. and Ph.D. degrees in electronics and communication engineering from the Politecnico di Torino, Turin, Italy, in 2011 and 2015, respectively. He is currently an Associate Professor with the EMC Group, Department of Electronics and Telecommunications, Politecnico di Torino. His research interests include the analysis of switching dc-dc converters, machine learning, and statistical simulation of circuits and systems.

Igor S. Stievano (Senior Member, IEEE) received the master's degree in electronic engineering and the Ph.D. degree in electronics and communication engineering from the Politecnico di Torino, Turin, Italy, in 1996 and 2001, respectively. He is currently a Professor of electrical engineering with the Department of Electronics and Telecommunications, Politecnico di Torino. From 2017 to 2021, he was the Vice Rector of Academic and Scientific Activities of the joint campus of the Politecnico di Torino in Uzbekistan, Turin Polytechnic University in Tashkent. He has authored or coauthored more than 130 papers published in international journals and conference proceedings. His current research interests include electromagnetic compatibility and signal integrity, with emphasis on the modeling and simulation of digital circuits, transmission lines, PLC channels, switching converters, the development of stochastic methods for the statistical simulation of circuits and systems, the compact modeling of electrical and gas networks via a complex network paradigm and simplified graph-based approaches. He was also the Program Co-Chair of the 20th and 21st IEEE Workshops on Signal and Power Integrity (SPI2016 and SPI2017).